

High Resolution X-Ray Spectroscopy Diagnostics of High Temperature Plasmas

To cite this article: E Källne *et al* 1985 *Phys. Scr.* **31** 551

View the [article online](#) for updates and enhancements.

Related content

- [X-ray Spectroscopy in Fusion Research](#)
E Källne and J Källne
- [High Resolution X-Ray Spectroscopy for Diagnostics of Single Tokamak Discharges](#)
E Källne and J Källne
- [Soft-X-ray spectroscopic diagnostics of laboratory plasmas](#)
C. De Michelis and M. Mattioli

Recent citations

- [X-ray diffraction patterns and diffracted intensity of K spectral lines of He-like ions](#)
Arun Goyal *et al*
- [High pressure X-ray emission spectroscopy at the advanced photon source](#)
Yuming Xiao *et al*
- [Measurement of the electron and ion temperatures by the x-ray imaging crystal spectrometer on joint Texas experimental tokamak](#)
W. Yan *et al*

High Resolution X-Ray Spectroscopy Diagnostics of High Temperature Plasmas

E. Källne and J. Källne

JET Joint Undertaking, Abingdon, England

E.S. Marmar and J.E. Rice

MIT Plasma Fusion Center, Cambridge, MA 02139, USA

Received January 28, 1985; accepted February 22, 1985

Abstract

This paper presents advances in the use of high resolution X-ray spectroscopy for the measurements of tokamak plasmas and the study of atomic processes. The measurements refer to H- and He- like spectra of Ar ($\lambda = 3.7$ to 4.2 Å) obtained with a new crystal spectrometer at the Alcator C tokamak. With record count rates of up to 0.5 MHz, time resolved spectroscopy of individual plasma discharge was demonstrated at the 20 ms time scale. In particular, the time evolution of ion and electron temperatures, $T_i(t)$ and $T_e(t)$, was determined and occurrences of transient plasma phenomena were recorded in discharges with deuterium pellet injection. X-ray line emission was for the first time observed along different chords through the plasma so as to determine the radial dependence of the principal plasma parameters $T_i(r)$ and $T_e(r)$. These radial scan data are shown to be of interest for identifying manifestations of underlying atomic processes and ion transport effects. On the basis of the present results we assess the future use of x-ray spectroscopy diagnostics to obtain extended information on the temporal and spatial dependences of the main plasma parameters together with new information on transient phenomena as well as on the neutral content of tokamak plasmas.

1. Introduction

The characteristic x-ray radiation from highly ionized atoms in tokamak plasmas has found rather extensive use as a means of diagnosing plasma conditions [1]. The main objective of high resolution x-ray spectroscopy measurements is often the determination of the plasma ion temperature (T_i) which is deduced from the Doppler broadening of emission lines [2]. For this purpose one needs well-separated x-ray lines which are provided by the simple spectra of few electron systems. Theoretically, the level structures of the H- and H-like atoms are well known, as are the atomic rates of recombination and ionization that determine the equilibrium balance of the ion charge states. This information together with atomic rates involving all relevant excited states has made it possible to calculate x-ray line intensities to a high accuracy as a function of plasma conditions [3]. Conversely, line ratio combinations have been identified that allow one to determine electron temperature (T_e) and density (N_e), for instance, from measured intensity ratios [4]. X-ray line spectra are therefore a potential source of multi-parameter information on plasma conditions which can be exploited with suitable instrumentation and techniques.

High resolution crystal spectrometers have been installed at several of the presently operating tokamak machines to measure the line emission in the energy range $h\nu = 2$ to 8 keV corresponding to the wavelength range $\lambda = 6$ to 1.6 Å. In this range appear the H- and He-like spectra of elements with $Z = 16$ to 28 and recent results have been reported on S, Cl, Ar, Ti, Cr and Fe

[5–12]. This selection of elements represents some common ambient impurities in the tokamak plasmas studied, apart from Ar which is deliberately introduced into the plasma [8, 11, 12]. The use of such seed elements is the preferred method for two main reasons: first, it allows one to choose the atomic charge Z of the ion that is most appropriate for optimizing the x-ray emission for given plasma conditions, especially with respect to T_e . Second, the ion seed concentration is a controllable parameter in contrast to that of the ambient plasma impurities, which tend to vary with plasma conditions.

Many x-ray spectroscopy measurements up till now have shown several limitations. Because of low data rates, and hence problems in achieving sufficient statistical accuracy, it has often been necessary to accumulate data over an extended time portion of a single discharge or to sum over several consecutive discharges. The data rate limitations arise for two principal reasons. An upper limit is, of course, set by the count rate capability of the detector. However, up to the detector limits, the data rate will be that of the photon flux in the spectrometer which is a function of the light collection efficiency (luminosity) of the instrument used and the line brightness of the x-ray emission that can be achieved under given plasma conditions. The line brightness produced by the plasma is limited by the ion concentration $C_I = N_I/N_e$. A related consideration is the fractional wavelength bandwidth of the spectrometer ($\Delta\lambda/\lambda$). By covering an extended wavelength band, more lines can be measured with a general improvement in the experimental precision. Another constraint has been the bulkiness of the instruments which limits their use to a fixed line of sight, usually through the plasma center.

A high performance spectrometer for tokamak measurements should combine the attributes of high luminosity (L), large fractional bandwidth ($\Delta\lambda/\lambda$) and good wavelength resolution ($\delta\lambda/\lambda$). On the practical side it should be versatile so as to allow selection of λ -range and line of sight, and flexible to allow easy change in these respects; both these aspects are enhanced if combined with the controlled introduction of seed elements to the plasma. Most instruments in use or planned for x-ray spectroscopy diagnostics are based on the Rowland circle Johann geometry, where very high resolution ($\delta\lambda/\lambda < 1/15000$) can be achieved partly because of the increased dispersion offered by the large size geometries usually used [6–9, 13, 14]. Another approach is based on the spectrometer geometry of von Hamos [15] utilizing small dimensions, moderately high resolution ($\delta\lambda/\lambda \geq 1/3000$), small wavelength dispersion and high performance detectors. In this case, capabilities of the position

sensitive x-ray detector with regard to detection area, spatial resolution and count rate become a crucial part of the spectrometer design.

In this paper we describe a compact and versatile high resolution x-ray spectrometer of the van Hamos geometry using the x-ray detector described in Ref. [16], together with a 1-MHz data acquisition system. The instrument was used on the Alcator C tokamak for measuring x-ray emission in the λ -range 3.7 to 4.2 Å, thus covering the H- and He-like spectra of argon. Argon was introduced into the plasma for this diagnostic experiment especially for testing the high count rate performance. Results are presented which demonstrate the recording of single shot, temporally resolved, x-ray spectra on a 10 to 20 ms time scale for various plasma conditions. Of the major plasma parameters, T_i was measured (using the Doppler broadening of the main x-ray lines of the H- and He-like spectra of argon), and T_e and N_e were determined from line intensity ratios. The temporal evolution of T_i , T_e and N_e were measured both for the standard gas fuelled Alcator plasmas and for those fuelled with pellet injection [17]. In addition, the first results on radial profiles of line brightness, T_i and T_e are reported as obtained on a shot-to-shot basis for both H- and He-like spectra. Moreover, the comparison of x-ray spectra from the center and the peripheral plasma regions is used to demonstrate interesting differences with regard to atomic population mechanisms and charge state abundance ratios. The paper is concluded with a discussion of x-ray diagnostics using high performance spectrometers and the envisaged capabilities to provide spatial and temporal characterization of the main plasma parameters of single tokamak discharges as well as new diagnostic information.

2. Experimental

2.1 The Alcator C Plasma

The Alcator C tokamak is a high field ($B_T < 13$ T) machine with liquid nitrogen cooled magnets [18]. The major and minor radii were 64 and 16.5 cm for most of the present measurements. During our measurements, the machine was operated at plasma currents of $I_p = 400$ –500 kA in either hydrogen or deuterium at $N_e = 1$ to $3 \cdot 10^{14} \text{ cm}^{-3}$ and $T_e = 1.3$ to 1.8 keV (due to Ohmic heating) in the plasma center. A typical Alcator discharge is illustrated in Fig. 1 which shows the time history of the current, the line average density, the central chord soft x-ray diode signal ($h\nu = 1$ –10 keV) and our x-ray signal ($h\nu \approx 3.0$ keV primarily due to Ar^{16+}). The plasma discharge lasts approximately 500 ms of which the middle 200 ms represent rather constant plasma conditions. Besides the ordinary gas fuelled plasma discharges we also studied discharges in hydrogen which were additionally fuelled through injection of deuterium pellets. The pellet raised the line average electron density by a factor of about 2; the resulting density profiles were more centrally peaked with an increase on the plasma axis of about a factor of 3 [17]. The pellet injection made drastic changes to the plasma conditions over the 1 to 100 ms time scale and offered an opportunity to study the time response of the x-ray spectra.

For the characterization of the plasma conditions, Alcator C has an extensive diagnostic instrumentation [18]. For the present x-ray spectroscopy measurements, we have made particular use of information on T_e from the x-ray continuum measured along a central chord, on $T_e(r)$ from the electron

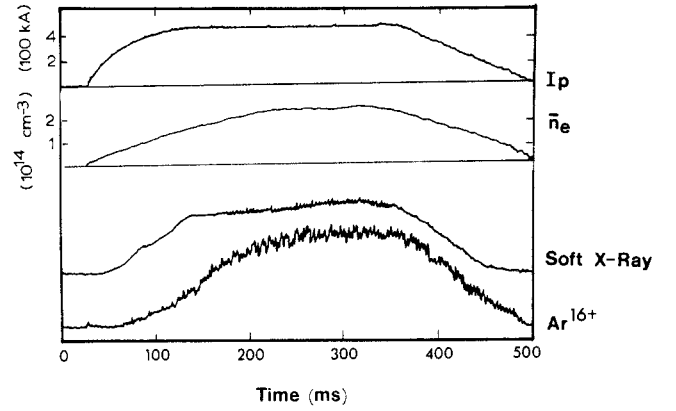


Fig. 1. The time evolution of plasma current (I_p) and line integrated density (N_e) of a typical Alcator C discharge. Also shown is the soft ($h\nu \approx 1$ keV) X-ray diode signal (I_x) and X-ray emission at $h\nu \approx 3.0$ keV (mainly from Ar^{16+}) detected by the spectrometer.

cyclotron emission (ECE) measurements, $N_e(r)$ from the far infrared interferometer measurements and Z_{eff} from the visible continuum measurements.

Our spectrometer viewed the plasma through a horizontal port using a 2×10 mm aperture in a $4\frac{1}{2}$ " conflat flange. A 125 μm thick vacuum window of beryllium was attached to the flange with epoxy. The spectrometer entrance slit was placed immediately outside the vacuum window at a distance of approximately 100 cm from the plasma axis. The lines of sight were always perpendicular to the toroidal axis; the chord height (d) from the plasma center was variable and could be set between plasma discharges. Radial scan measurements were obtained from sequences of similar discharges.

In previous measurements at Alcator C, we observed the emission from S and Cl at ion densities of $N_i < 10^9$ – 10^{10} cm^{-3} i.e. concentrations of $C_i = N_i/N_e = 10^{-4}$ – 10^{-5} for He-like charge states [10]. The densities of these ambient impurities, however, vary with plasma parameters as well as with wall and limiter conditions. For the results reported here, argon was seeded into the plasma so that N_i was controllable and could be readily adjusted to maintain the x-ray signal at the desired level. Argon was chosen because it is easy to use and it has a suitable ionization potential for the He-like charge state which gives maximum emission at an electron temperature (T_m) of 1.8 keV. The argon gas was introduced into the plasma through a piezo electric valve which was open for about 10 ms, starting 20 ms into the discharge. The argon subsequently recycles, so that a steady x-ray signal is obtained for the constant portion of the discharge. The plasma seeding technique makes the x-ray measurements an active diagnostic, and the seeding levels used are comparable to or below the levels of intrinsic impurities, and do not significantly perturb Z_{eff} or the radiated power. A tolerable upper limit of C_i can be defined as the value where the concentration of this medium Z element gives a certain contribution to the central radiated power loss of the plasma [19], say 5%. For a typical Alcator plasma ($N_e = 2 \times 10^{14} \text{ cm}^{-3}$ and $T_e = 1.4$ keV) the concentration of argon should be less than $C_i = 10^{-3}$.

Given an ion density N_i in a plasma of electron density N_e the x-ray volume emissivity is

$$E = N_i Q N_e \quad (1)$$

Here it is assumed that the population rate for the upper state

of the transition is Q and that the resonance line is populated by electron impact excitation from the ground state. Experimentally, the line emission would appear with a brightness

$$B = \frac{1}{4\pi} \int E \times dl \approx \frac{1}{4\pi} Q I N_I N_e \quad (2)$$

where l is the thickness of the radiating plasma. For the Alcator conditions $N_e = 2 \cdot 10^{14} \text{ cm}^{-3}$, $T_e = 1.4 \text{ keV}$ and $l \simeq 20 \text{ cm}$, the $n = 2$ to $n = 1$ resonance line of He-like Ar (assuming $C_I = 10^{-4}$ and using $Q = 3.7 \cdot 10^{-12} \text{ cm}^3/\text{s}$ from Ref. [20]) gives a line brightness value of

$$B = 2.10^{13} \text{ photons/sr/cm}^2/\text{s}$$

which gives a line count rate of (n_L) photons/s

$$n_L = B \cdot L \quad (3)$$

depending on the spectrometer luminosity L . From Eq. (3) we see that in order to achieve a count rate of $n_L = 10^5 \text{ s}^{-1}$, the spectrometer must have $L > 10^{-8} \text{ sr} \cdot \text{cm}^2$. This design goal for plasma spectroscopy is rather independent of ion species since Q varies only slowly with Z in the range of practical interest ($Z = 16\text{--}30$) and since Z can be chosen so that $T_m(Z) = T_e$. However, the line count rate is sensitive to the electron density product $N_I N_e$ in Eq. (2).

2.2 The Spectrometer

For extended x-ray sources such as tokamak plasmas, the conventional spectrometer has been of the Johann geometry. It uses a Rowland circle geometry, where the crystal is curved in the dispersive direction, and has been chosen to provide large dispersion and high luminosity. In our case, we have been able to relax the dispersion requirement, owing to the characteristics of the new x-ray detector and still achieve high resolution. We have chosen a spectrometer based on the von Hamos geometry [15]. Although primarily used for point source applications [21], the von Hamos geometry is suitable for extended sources and distinct advantages present themselves in the practical spectrometer implementation for achieving large bandwidth, large spectral scanning range, high resolution including off-axis sources, high luminosity, compact dimensions, and small entrance window and viewing aperture to the plasma.

The spectrometer geometry of von Hamos is characterized by simple optics. It uses a crystal which is flat in the diffractive direction and cylindrically curved in the non-dispersive direction as shown in Fig. 2. This means that an object (defined by the entrance slit) in the plane through the cylinder axis will be imaged (as recorded by the detector) on the same plane after the diffraction; i.e., each position along the cylinder axis represents a certain wavelength defined (in first order) by the lattice spacing ($2d$) and the Bragg angle (θ) through $\lambda = 2d \sin \theta$. The detector is positioned perpendicular to the incident photon direction in order to optimize the conditions for the wavelength determination; the vertical focussing is compromised in this position but transverse spatial resolution was not required in this measurement. An important consequence of the transverse focussing is the increased light collection efficiency per unit detector height.

For the present experiment, we have built a small spectrometer using a quartz crystal ($25 \times 25 \text{ mm}$) with a radius of curvature of $R_c = 50 \text{ cm}$. The lattice parameter of the $10\bar{1}1$

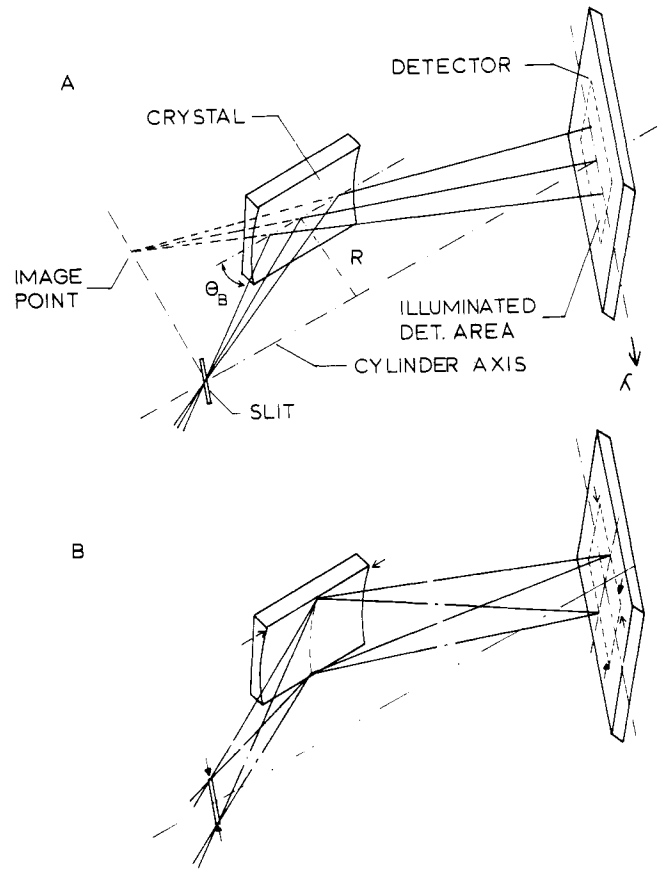


Fig. 2. Schematics of the dispersive (A) and focussing (B) characteristics of the crystal spectrometer used.

plane is $2d = 6.687 \text{ \AA}$ so that for the spectral scanning range of $\theta = 30$ to 37° ($\theta_0 = 35.5^\circ$) the wavelength range was $\lambda = 3.3$ to 4.2 \AA . The bandwidth is defined by the projected length of the crystal ($l_c \sin \theta$) and the distance to the entrance slit $d_{sc} = R_c / \sin \theta$, i.e. $\Delta\lambda/\lambda = l_c \sin^2 \theta / R_c = 1.5\%$ [22]. This allowed us coverage of the entire spectrum of either H- or He-like argon. Change of λ -ranges was accomplished between shots by adjusting the angles of the crystal and the exit arm of the spectrometer on which the detector was attached.

The spectrometer luminosity is defined as

$$L = \epsilon A d \Omega \quad (4)$$

where the efficiency factor (ϵ) is a product of the detector efficiency (ϵ_d), crystal reflectivity (ϵ_c) and photon transmission in foil (ϵ_t), and A is the slit area ($w_s \cdot h_s$). The solid angle subtended by the spectrometer $d\Omega$ is

$$d\Omega = \rho \frac{h_c}{d_{sc}} \quad (5)$$

i.e., the product of the crystal resolving power ρ and the aperture angle of the crystal. With $h_s = 10 \text{ mm}$, $w_s = 0.2 \text{ mm}$, $\rho \sim 1/5000$ and $\epsilon = 0.3$ together with the values as given above, we obtain $L = 4 \cdot 10^{-8} \text{ sr} \cdot \text{cm}^2$.

Although the bandwidth and luminosity values were adequate for the present explorative study, principally to test the important detector count rate capability, these do not represent an optimum design. Actually both these values can be increased substantially by utilizing larger crystal, detector and slit areas together with thinner windows to increase the photon transmission. A recent study of a practical design indicated that

$\Delta\lambda/\lambda = 10\%$ and $L = 3 \cdot 10^{-6} \text{ sr} \cdot \text{cm}^2$ [23] are achievable with this spectrometer geometry. This particular optimization was chosen to allow simultaneous measurement of the H- and He-like spectra of Ar (or other elements) at line count rates in excess of 10^6 s^{-1} for ion concentrations as low as $C_I = 10^{-5}$.

The compact spectrometer was free-standing from the tokamak which presented measuring flexibility with minimal requirements of port access. The angle of elevation was variable around a pivot at the spectrometer entrance and was used to select the line of sight through the plasma as defined by the chord height distance (d) from the plasma axis; the chord height resolution was $\Delta d = 3 \text{ cm}$ (FWHM). The present radial scan measurements were made on a shot-to-shot basis but simultaneous multi-chord measurements are envisaged in the future by using an array of five or more spectrometers.

2.3 The Detector

For the photon detection, a new multi-wire gas proportional counter has been used. It is filled with krypton/ethane gas at 1 atm. and has a detection area of $35 \times 10 \text{ mm}^2$. The position determination is obtained from an LC delay line readout of the induced cathode pulse. The delay line is laid out on a printed circuit board and is at the same time the cathode plane. The detector has very low characteristic impedance (200Ω), short pulse length ($\sim 6 \text{ ns}$) and a signal transit time of less than 28 ns corresponding to 0.8 ns per 1 mm of detector length. This provides for short duration detector events and hence high count rate capability. The design of the detector has been described earlier and here we merely summarize some details pertinent to its use in the present experiment [16].

The spatial resolution as a function of photon energy was tested with a well collimated fluorescent radiation source from secondary anodes (Si, Ca, Sc and Cr) in an x-ray tube [16]. The tests showed no obvious degradation of the resolution with decreasing energy down to about 1.5 keV , i.e., the spatial resolution was $\Delta x \sim 80 \mu\text{m}$ or better; the entrance window ($76 \mu\text{m}$ thick Be) prevented tests below this photon energy. This implies that the signal amplitude has to be at least below that of 1.5 keV photons to reduce the signal to noise ratio to levels where the position resolution starts to be noise limited. This confirms the earlier finding [16] that noise makes no significant contribution to the spatial resolution of the detector for 3 keV photons which is important for maintaining the high resolution at high local count rates.

On the tokamak, the high count rate performance of the detector was tested by varying the argon concentration and thereby systematically changing the photon flux. In this way, detector count rates consistent with the maximum rate of the present data acquisition system (i.e., 1 MHz) were demonstrated; the theoretical detector rate limit is $> 20 \text{ MHz}$. Even more important is the local count rate for which we have recorded values up to 200 kHz/mm (i.e., over a single x-ray emission line) with no degradation in the observed line width; i.e., the spatial resolution was better than $150 \mu\text{m}$ at 200 kHz/mm corresponding to 40 kHz/mm for each anode wire. High count rates will cause positive space charge build up around the anode wire resulting in a decrease of the detector gain. At 40 kHz/mm , the expected [24] loss in gain is about a factor of 2 and there would be a corresponding decrease in the signal to noise ratio. We have already noted that a factor of 2 change in this ratio has no observable effect on the spatial resolution of $80 \mu\text{m}$ and

for a required resolution of $\Delta x \leq 150 \mu\text{m}$ we estimate that the signal to noise ratio can be allowed to decrease at least a factor of four (corresponding to 80 kHz/mm per anode wire) so that the theoretical local count rate limit of our detector is $n_L > 0.4 \text{ MHz/mm}$ using five anode wires.

The position read-out and the data acquisition system were realised with fast LeCroy CAMAC electronics. The detector timing pulses were recorded with a time-to-digital converter (TDC model 4202) used on a 78 ps/channel time scale. The time resolution of TDC was measured to be 280 ps (FWHM) which is not quite good enough to avoid contributions to the instrumental resolution. The measured time histograms representing the position spectra were stored in a histogramming memory module (LeCroy 3588) before being read into a VAX 11/780 computer. For each plasma discharge, up to 64 spectra were stored, each comprising 512 channels of memory and representing 10 ms accumulation time.

2.4 Spectrometer Performance

Examples of data obtained with the new spectrometer system are shown in Fig. 3. Presented in a sequence of 24 x-ray line spectra of He-like Ar $n = 2$ to $n = 1$ transitions recorded during a single Alcator discharge each representing an accumulation time of 20 ms . The time evolution of the intensities of the spectral lines is displayed in the three-dimensional plot of Fig. 4. This shows that the intensity increases towards the middle of the discharge so that in spectrum number 12 of Fig. 3 one reaches a total instantaneous count rate of 500 kHz and a local count rate of $n_L = 200 \text{ kHz}$ in the strongest line. No deterioration in resolution due to high count rate could be observed and there was no shift in peak position either for well separated peaks or for adjacent ones. This line count rate corresponds to a statistical accuracy of $\pm 1.5\%$ in the line intensity (assuming 20 ms time bins). If $\pm 15\%$ is the minimum accuracy required (corresponding to $n_L > 2 \text{ kHz}$), the measurement has a dynamic range of a factor 100.

3. Theoretical background and data analysis

The H-like spectrum consists of the two resonance lines W_1 and W_2 belonging to the $2P_{3/2, 1/2}$ states (see Table I for a summary). Besides these principal lines, there are satellite lines which arise from an additional electron occupying an $n = 2$ orbital or $n > 2$ orbital. The strongest $n = 2$ satellites are J and T, which appear well separated in the spectrum and three other ones A, B and Q can also be identified (see Fig. 5 and Table I). The $n \geq 3$ satellites form foot hills to the resonance lines. The He-like spectrum has four principal lines due to the resonance line (w), the intercombination (x and y) and the forbidden transition (z) belonging to the $1s2p \ ^1P_1$, $1s2p \ ^3P_{1,2}$ and $1s2s \ ^3S_1$ states (see Table II for a summary). The strongest satellite lines are k and q (see Figs. 6 and 7). The lines J, T and k form one class of satellites since their corresponding upper states are doubly excited and are formed only through dielectronic recombination on the H- and He-like ground states, respectively, while the q line is a resonance transition of the Li-like charge state and is thus populated in the same way as w and $W_{1,2}$.

In the center of the plasma, the conditions exist for obtaining abundance ratios of the ion charge states that are close to the balance due to the atomic ionization and recombination rates (coronal equilibrium). The x-ray line intensities of the H-

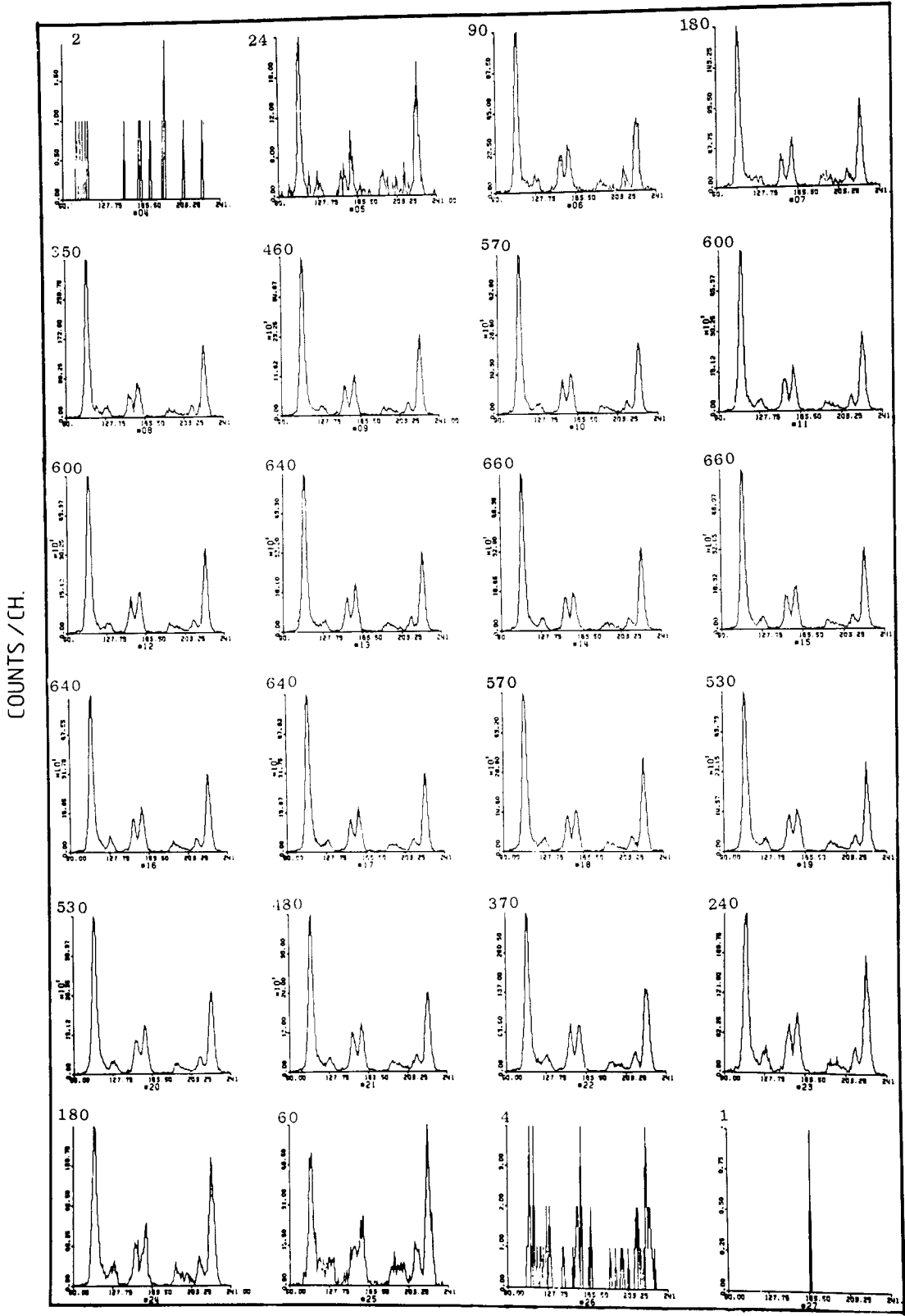


Fig. 3. Sequence of He-like Ar spectra. Each spectrum was recorded over 20 ms from the beginning (the upper left one) to the end of the discharge. The y-axis gives the number of counts per channel (with the full scale value indicated) and the x-axis spans 150 channels; see Fig. 6 for an explanation of spectral details.

and He-like spectra can be calculated for given plasma conditions assuming coronal equilibrium where the following line intensity ratios are principal functions of the indicated plasma parameters:

J/W
 w/W

T_e
 $T_e [N_{He}/N_H]$

k/w
 q/w
 $G = (x + y + z)/w$
 $R = z/(x + y)$

T_e
 $T_e [N_{Li}/N_{He}]$
 T_e
 N_e

In the cases of w/W and q/w one must rely on the coronal

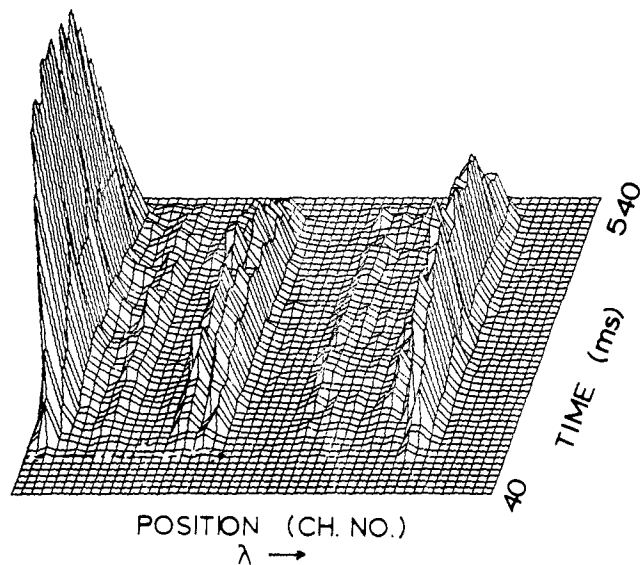


Fig. 4. Plot of the measured X-ray emission of He-like Ar as a function of wavelength and time; the time bin size is 20 ms and the position is displayed in bins of four channels.

equilibrium assumption to deduce T_e from the measured line intensity ratios. A more detailed discussion of the dependences of these line intensity ratios or plasma parameters can be found in Refs. [1, 4, 11, 26, 27, 28].

In the peripheral region of the plasma, there is a strong gradient in the radial profiles of $T_e(r)$ or $N_e(r)$, and the abundance ratios can be much shifted from those of coronal equilibrium by ion transport. For instance, the Ar $N_{\text{H}}/N_{\text{He}}$ ratio of the coronal equilibrium should decrease rapidly with minor radius for $r \geq 10$ cm in Alcator C because of the fall-off in $T_e(r)$. However, ion transport effects would tend to moderate the radial rate of decrease in $N_{\text{H}}/N_{\text{He}}$ given by coronal equilibrium alone. The lines W, w and q give rather direct information on ion abundance ratios. In the central plasma, where all three transitions are populated principally by impact excitation, the relative intensities $I_{\text{W}}/I_{\text{w}}/I_{\text{q}}$ will reflect the abundance ratios $N(\text{Ar}^{17+})/N(\text{Ar}^{16+})/N(\text{Ar}^{15+})$. In the peripheral plasma regions where recombination is the dominant population mechanism for W and w, the ratio $I_{\text{W}}/I_{\text{w}}$ should indicate the abundance ratio $N(\text{Ar}^{18+})/N(\text{Ar}^{17+})$. Clearly, in order to extract quantitative information from these line intensities one must perform a detailed computation of the ionization-recombination rate balance and the ion transport effects which will be presented in a forthcoming paper [29]. For the qualitative

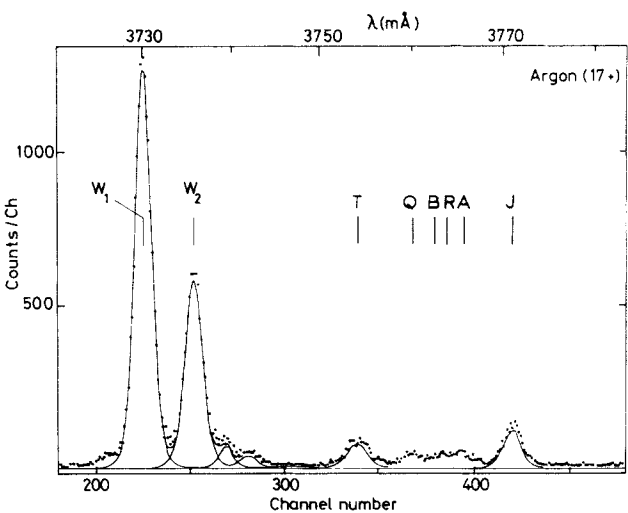


Fig. 5. The spectrum of H-like Ar accumulated over ten plasma discharges of 200 ms time integration. The plasma conditions were $\bar{N}_e = 2.3 \cdot 10^{14} \text{ cm}^{-3}$, and $T_e = 1450 \text{ eV}$.

discussion of the present paper it will suffice to observe that the $N(\text{Ar}^{17+})/N(\text{Ar}^{16+})$ and $N(\text{Ar}^{18+})/N(\text{Ar}^{17+})$ ratios are enhanced above the value of balance between recombination and ionisation in the peripheral region of the plasma.

Because of the radial profiles of tokamak plasma, especially $T_e(r)$ and its effects on abundance ratios (for instance $N_{\text{H}}/N_{\text{He}}$), each plasma encompasses the conditions for the H- and He-like spectra to be populated in turn by different atomic excitation mechanisms. Specifically, in the plasma center with $T_e \approx 1.5$ keV in our case, the principal population mechanisms for the Ar spectra are electron impact excitation and dielectronic recombination. Because of the differences in temperature dependence of the corresponding rates (the ratio of satellite to resonance line intensities is $I_{\text{s}}/I_{\text{r}} \sim 1/T_e \exp(-E/T_e)$ where E is the excitation energy) the satellites will increase in relative importance with increasing radius. However, both these mechanisms involve excitation of a 1s electron to the $n = 2$ orbital so in absolute terms the rates will decrease strongly with decreasing T_e (and hence with increasing r) because of the exponential T_e dependence $\exp(-E/T_e)$. Radiative recombination, $e + \text{Ar}^{17+} \rightarrow (\text{Ar}^{16+})^* + \gamma$ or $e + \text{Ar}^{18+} \rightarrow (\text{Ar}^{17+})^* + \gamma$, involves no excitation and its rate increases with falling T_e ; note that only the principal lines of the H- and He-like spectra can be populated by recombination. Therefore, the radiative rate will surpass those of electron impact excitation and dielectronic recombination at some critical value of the ratio $N_{\text{H}}/N_{\text{He}}$ (assuming enhancement to above the coronal equilibrium) and T_e as some critical radius is reached [30]. A competing process in this case is charge transfer recombination involving the neutrals in the plasma, $\text{D} + \text{Ar}^{17+} \rightarrow (\text{Ar}^{16+})^* + \text{D}^+$ (assuming a deuterium plasma). The charge transfer rate would exceed the radiative rate, at a critical neutral concentration of $N_0/N_e \gtrsim 10^{-5}$. This would occur at some certain radius since N_0/N_e increases exponentially towards the plasma edge where it could reach values of $N_0/N_e \sim 10^{-3}$ [31].

The measured spectra were analysed with a least square line-fit program. From this we extracted the relative intensities of the resolved lines of the spectra. The z-line of the He-like spectrum is merged with the satellite line j. The intensity of j was estimated as 1.3 times the k line intensity and subtracted from the sum of z + j measured [11, 25]. The line profile used

Table I. Wavelengths of the principal lines and the strongest dielectronic satellites in the H-like spectrum of Ar

Key	Transition	$\lambda(\text{\AA})^1$
W_1	$1s\ ^2S_{1/2} - 2p\ ^2P_{3/2}$	3.7300
W_2	$1s\ ^2S_{1/2} - 2p\ ^2P_{1/2}$	3.7352
T	$1s2s\ ^1S_0 - 2s2p\ ^1P_1$	3.7544
K	$1s2p\ ^3P_2 - 2p^2\ ^1D_2$	3.7557
Q	$1s2s\ ^3S_1 - 2s2p\ ^3P_2$	3.7603
B	$1s2p\ ^3P_1 - 2p^2\ ^3P_2$	3.7626
R	$1s2s\ ^3S_1 - 2s2p\ ^3P_1$	3.7639
A	$1s2p\ ^3P_2 - 2p^2\ ^3P_2$	3.7657
J	$1s2p\ ^1P_1 - 2p^2\ ^1D_2$	3.7709

¹ Theoretical values from ref. [25]

Table II. Wavelengths of the principal lines and the strongest satellites due to dielectronic recombination and inner shell excitation (denoted *) in He-like Ar

Key	Transition	$\lambda(\text{\AA})^1$
w	$1s^2\ ^1S_0 - 1s2p\ ^1P_1$	3.9482
m	$1s^2\ 2p\ ^2P_{3/2} - 1s2p^2\ ^2S_{1/2}$	3.9562
x	$1s^2\ ^1S_0 - 1s2p\ ^3P_2$	3.9649
s	$1s^2\ 2s\ ^2S_{1/2} - 1s(2s2p^1P)^2P_{3/2}$	3.9669
t	$1s^2\ 2s\ ^2S_{1/2} - 1s(2s2p^1P)^2P_{1/2}$	3.9677
y	$1s^2\ ^1S_0 - 1s2p\ ^3P_1$	3.9683
q*	$1s^2\ 2s\ ^2S_{1/2} - 1s(2s2p^1P)^2P_{3/2}$	3.9806
r	$1s^2\ 2s\ ^2S_{1/2} - 1s(2s2p^1P)^2P_{1/2}$	3.9827
a	$1s^2\ 2p\ ^2P_{1/2} - 1s2p^2\ ^2P_{3/2}$	3.9852
k	$1s^2\ 2p\ ^2P_{1/2} - 1s2p^2\ ^2D_{3/2}$	3.9892
j	$1s^2\ 2p\ ^2P_{3/2} - 1s2p^2\ ^2D_{5/2}$	3.9932
z	$1s^2\ ^1S_0 - 1s2s\ ^3S_1$	3.9934
1*	$1s^2\ 2s^2\ ^1S_0 - 1s2s^2\ 2p\ ^1P_1$	4.0096
2	$(1s^2\ 2s2p\ ^3P_1 - 1s(2p^2\ 2s^4P)\ ^3P_1)$	4.0176
	$(1s^2\ 2s2p\ ^3P_0 - 1s2s2p^2\ ^3D_1)$	4.0179
	$(1s^2\ 2s2p\ ^3P_2 - 1s(2p^2\ 2s^4P)\ ^3P_2)$	4.0180
3	$1s^2\ 2s2p\ ^3P_1 - 1s2s2p^2\ ^3D_2$	4.0192
4	$1s^2\ 2s2p\ ^3P_2 - 1s2s2p^2\ ^3D_3$	4.0219
5	$1s^2\ 2s2p\ ^1P_1 - 1s2s2p^2\ ^1D_2$	4.0291

¹ Theoretical values from ref. [25]

was nearly Gaussian (Voigt profile with a small Lorentzian contribution) and this was kept constant in the analysis of a spectrum except for the height and width. The width (Γ) was generally determined by the fit to the strongest peak in the spectrum and once determined, the same value was subsequently used to fit the entire spectrum, consisting of at least four individual lines in the H-like spectrum and ten lines in the He-like spectrum. The wavelengths of these lines are well known from calculations and this information was used for the wavelength scale calibration of the measured position spectra. Γ could thus be expressed in terms of $\Delta\lambda$ so that the Doppler broadening due to the thermal ion temperature T_i (in units of eV) of an ion with mass M (in amu) is determined by

$$T_i = \frac{M \cdot \Delta\lambda^2}{C^2 \cdot \lambda^2} - T_0 \tag{6}$$

where $C = 7.7 \cdot 10^{-5}$ and T_0 is the known instrumental resolution expressed as temperature (in eV). One can note in this context that the x-ray measurements can be performed in such a way as to obtain an absolute determination of wavelengths which in principal allows one to study Doppler line shifts corresponding to net ion motions down to the level of 10^6 cm/s as discussed in Ref. [32].

4. Results

4.1 The H-like Spectrum

A typical example of results on the H-like Ar spectrum is shown in Fig. 5. The spectrum is dominated by the resonance lines with some low intensity $n \geq 3$ satellites appearing in the same wavelength region. Although some of these are blended with the resonance lines, their contribution to the apparent width and intensity of the resonance lines used is of no practical consequence for extracting diagnostic information. A number of $n = 2$ satellites appear in the region $\lambda > 3.750$ Å of which T, Q, B, R, A and J can be identified (ref. [25] and Table I). The dominant J and T satellites are well resolved and most suitable for determining T_e .

4.2 The He-like Spectrum

Fig. 7 shows an example of a He-like Ar spectrum accumulated at high count rate during 20 ms resulting in sufficient statistical accuracy for all but the low intensity satellite lines. An accumulation time of 200 ms gave the spectrum shown in Fig. 6, where one can distinguish the four principal lines, the extended distribution of $n \geq 3$ satellites on the long wavelength side of the resonance line and several distinguishable contributions from $n = 2$ satellites. One can also observe a very weak contribution of spectroscopic interest in the region $\lambda = 4.01$ to 4.03 Å (Fig. 8). These lines do belong to Ar transitions because of their observed correlation with the argon density. They therefore ought to belong to $n = 2$ to $n = 1$ satellites transitions in Ar^{14+} which are predicted [25] to fall in this λ range. The five strongest satellite lines due to inner shell excitation and dielectronic recombination according to theory are given in Table II. The main concentrations of intensity found in the experiment at $\lambda = 4.014, 4.017$ and $4.023 (\pm 0.0015)$ Å occur close to the predicted locations of the strongest dielectronic satellites, while there seems to be no experimental counterpart to the predicted satellite populated by inner shell excitation; the latter line would be the transitions in Ar^{14+}

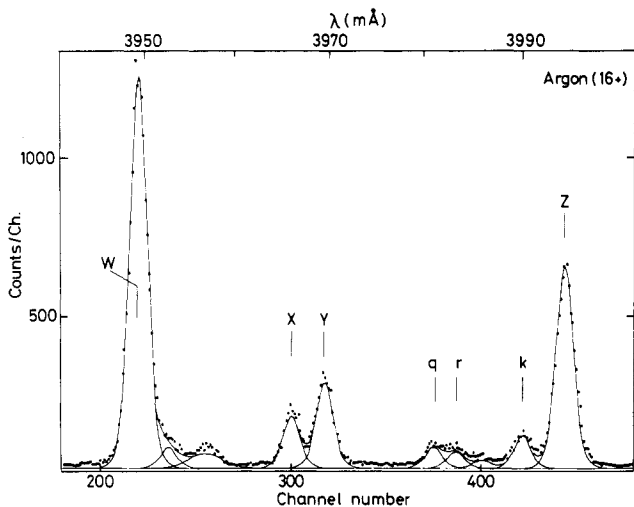


Fig. 6. The spectrum of He-like Ar accumulated over 200 ms of a single discharge with the plasma conditions of $\bar{N}_e = 2.9 \cdot 10^{14} \text{ cm}^{-3}$ and $T_e = 1250 \text{ eV}$.

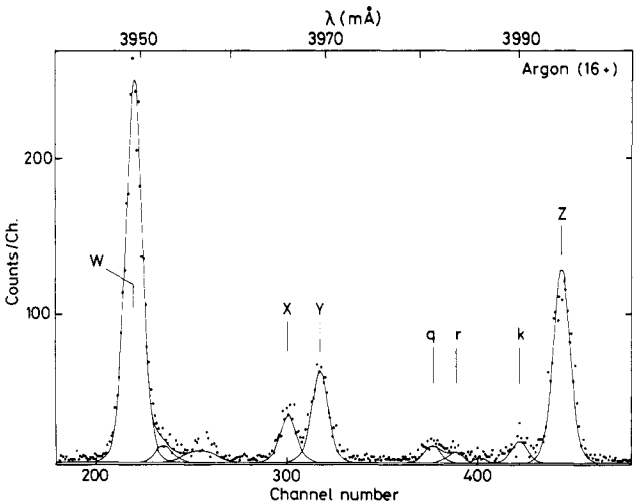


Fig. 7. The spectrum of He-like Ar accumulated for 20 ms over a single plasma discharge (same as for Fig. 6).

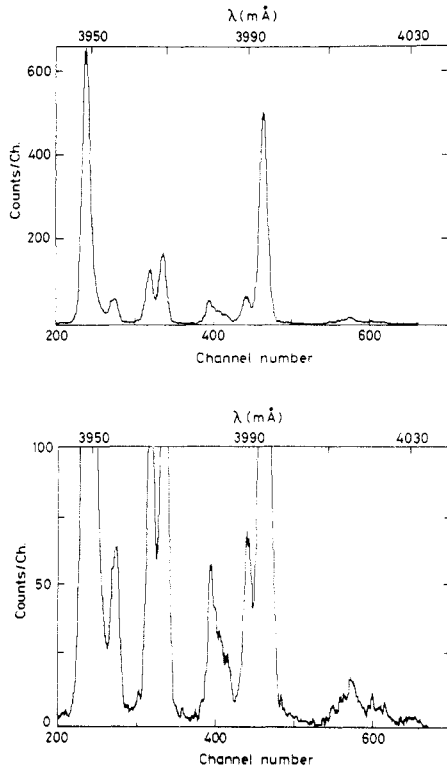


Fig. 8. The He-like Ar spectrum from a sum of four discharges over a 60 ms integration time with $\bar{N}_e = 1.5 \cdot 10^{14} \text{ cm}^{-3}$ and $T_e = 1500 \text{ eV}$ showing enhanced satellite intensities in the regions of $\lambda = 3.970\text{--}3.990 \text{ Å}$ (Ar^{15+}) and $\lambda = 4.015\text{--}4.035 \text{ Å}$ (Ar^{14+}).

that correspond to the q, w and $W_{1,2}$ lines in Ar^{15+} , Ar^{16+} and Ar^{17+} , respectively. Since the Ar^{14+} transitions have both a low intensity and a complex line structure, the lines of diagnostic interest here are the principal lines (w, x, y and z) of Ar^{16+} and satellite lines k and q of Ar^{15+} .

4.3 Ion Temperature (T_i)

Along central chords of observation, the ion temperature, T_i , was extracted from the width of the resonance lines of the H- or He-like spectra. Since the x-ray emission is peaked at the plasma center (see section 4.6) the measured T_i refers to the same region. An example of the measured time development of T_i is shown in Fig. 9, with a time resolution of 40 ms. The measurement was done for a typical Alcator discharge whose time histories of I_p , N_e and the x-ray signals I_x and I_{Ar} are shown in the lower panel of Fig. 9. A maximum T_i of 1.1 keV was reached in this discharge compared to a corresponding T_e value of 1.45 keV as determined from x-ray bremsstrahlung measurements. A discussion of the correlation between measurements of $T_i(t)$ and $T_e(t)$ is presented in Section 4.5. A comparison between our results on $T_i(t)$ and that of the neutral particle analyser is shown in Fig. 10 for a deuterium discharge with deuterium pellet injection. The two measurements show good agreement.

The ion temperature was measured for different chords of observation where the distance (d) from the plasma axis changed from $d = -7 \text{ cm}$ to $d = 12.7 \text{ cm}$; the maximum d corresponds to 75% of the limiter radius. In this case, we used the line width data from all four principal lines of the He-like spectrum. In this way, the statistical accuracy can be improved; this is especially important for the large radii, where the intensity is low and the intercombination and forbidden lines

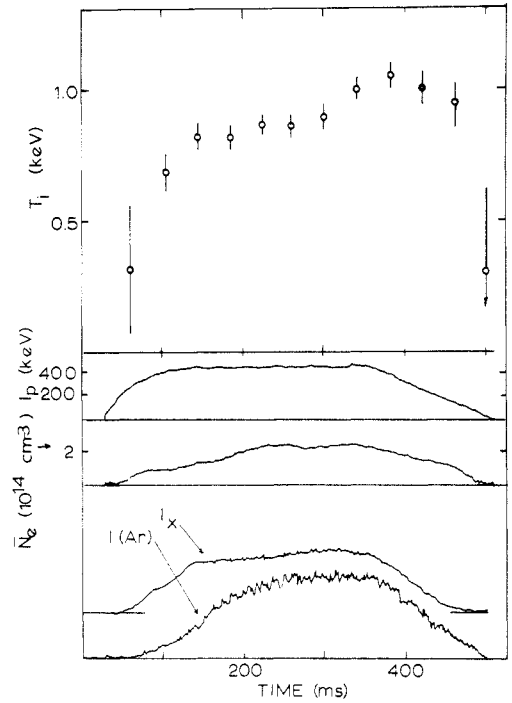


Fig. 9. The measured ion temperature (T_i) vs time for a typical Alcator C plasma discharge. Comparison is made with time traces for plasma current (I_p) and density (\bar{N}_e) as well as with the x-ray signals from the spectrometer (the He-like Ar spectrum, $I(\text{Ar})$) and a diode counter ($h\nu \geq 1 \text{ keV}$, I_x).

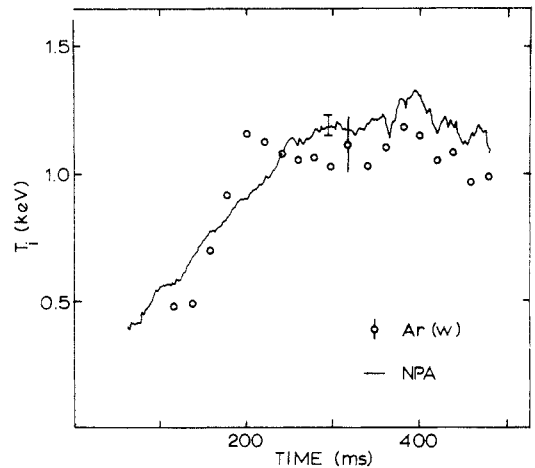


Fig. 10. Comparison of results on ion temperature from the present measurement and from the neutral particle analyser experiment. The plasma conditions were $\bar{N}_e = 3.2 \cdot 10^{14} \text{ cm}^{-3}$ and $T_e = 1450 \text{ eV}$ before the injection of a pellet at time 200 ms.

are stronger than the resonance line [31]. The results on the radial temperature profile $T_i(d)$ are shown in Fig. 11. For the data at large d , it is important to note that the errors shown reflect the statistical uncertainties typical for recording of a single discharge. Furthermore, $T_i(d)$ is the experimentally measured profile which mimics the radial profile $T_i(r)$ because of the center weighting along the line of sight mentioned above. An Abel inversion was not attempted here but will be presented in the quantitative analysis to be published in a subsequent paper [29]. Although no other data exist on $T_i(r)$, comparison can be made with $T_e(r)$ from ECE measurements (Fig. 11). This shows that the T_i values are generally lower than those on T_e with an

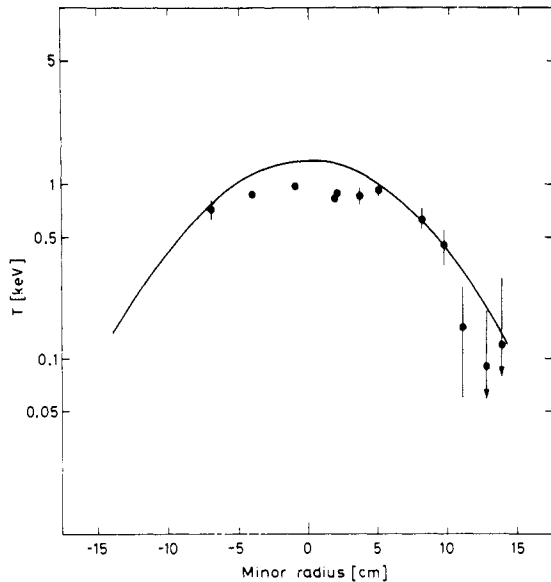


Fig. 11. Ion temperature profile measured as a function of the distance from the plasma axis (d). The solid curve is $T_e = T_0 \cdot \exp -(R/a)^2$ with $T_0 = 1.45$ keV and $a = 9.2$ cm.

overall scale factor of $T_i/T_e \approx 0.8$ and a possible radial difference in that the two temperatures are more similar at the larger radii.

4.4 Electron Temperature

The time dependence of T_e obtained from the line ratio k/w , is shown in Fig. 12, together with $T_e(t)$ from ECE. We see that our results and the ECE data show the same time development although there seems to be a systematic difference in magnitude. The normalization of the T_e scale of the x-ray data could be directly assessed with simultaneous measurements of H- and He-like spectra, and higher accuracy could in this way be achieved as well.

The line ratio k/w was measured as a function of d , from which we deduced an apparent radial temperature profile $T_e(d)$. The results are shown in Fig. 13 and compared with $T_e(r)$ from ECE. It should be noted that the T_e deduced from the x-ray data should be limited to the region $d \leq 8$ cm, where we can assume the satellites are populated by dielectronic recombination. Just outside $d \approx 8$ cm there is still an apparent agreement with $T_e(r)$ from ECE but at some point the x-ray data will be affected by the large gradients in $T_e(r)$ and by the change of atomic population mechanisms.

4.5 Discharges with Pellet Injections

Some of our x-ray measurements were made during early tests with the pellet injector on Alcator C. The pellets have a drastic effect on the N_e and T_e of the plasma; in global terms this can be seen from the time traces of $N_e(t)$ as well as from the soft x-ray and argon line emission intensities $I_x(S)$ and $I_x(\text{Ar})$ (Fig. 14). The I_x signals drop at the time of the injection but recover to the pre-injection level within 15 to 25 ms depending on whether the $I_x(\text{Ar})$ signal refers to the H- or He-like spectra; this difference can be related to the longer ionization time of Ar^{17+} (Fig. 14b) compared to Ar^{16+} (Fig. 14a). The $I_x(\text{Ar})$ signal continues to rise over a period of 100 ms to reach a maximum some four to five times higher than the pre-pellet level. The Ar density should be unaffected by the pellet, so that the $I_x(\text{Ar})$ signal should initially vary due to changes in the

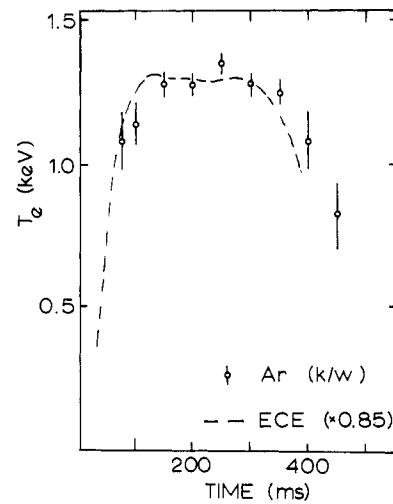


Fig. 12. The measured electron temperature as a function of time compared to results from ECE measurements; the latter were normalised to x-ray bremsstrahlung measurements.

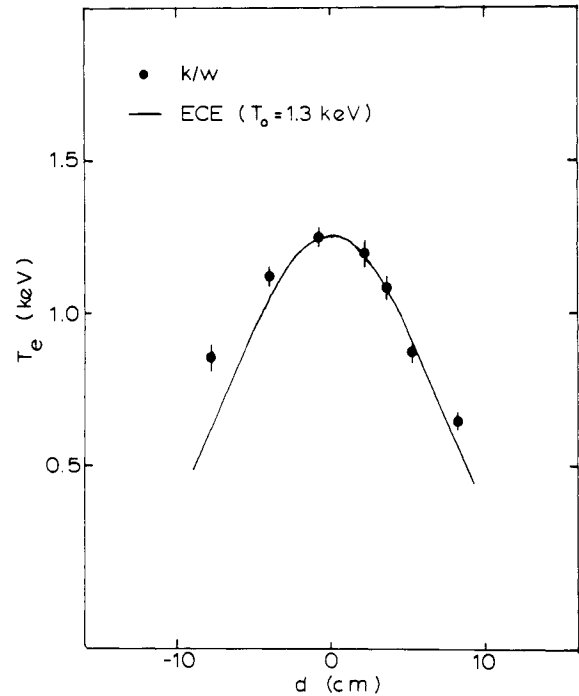


Fig. 13. The measured electron temperature as a function of distance from the plasma axis (d) compared with the radial profile $T_e(r)$ of ECE measurements.

central electron temperature and density directly caused by the pellet. However, the large sudden decrease in the central N_{Ar}/N_e ratio would be re-adjusted by ion transport at the $\gtrsim 1$ ms time scale and by ion recycling at a somewhat longer time scale. The rise in the I_x signal after the pellet injection can therefore be related to the increase mainly in N_e but also in T_e ; superimposed on this is the increase in N_{Ar}/N_e with time, due to transport and recycling. The changes in N_e and T_e can be separately seen in the present time resolved spectroscopy data.

The response of the x-ray line emission to the pellet injection can be seen in the measured time dependence of the line intensity ratios J/W , k/w , q/w , $G = (x + y + z)/w$, $R = z/(x + y)$ and the line widths Γ_w and Γ_w , (Fig. 15). It should be noted that the H- and He-like spectra are taken from different sets of similar discharges. To improve the statistics of these

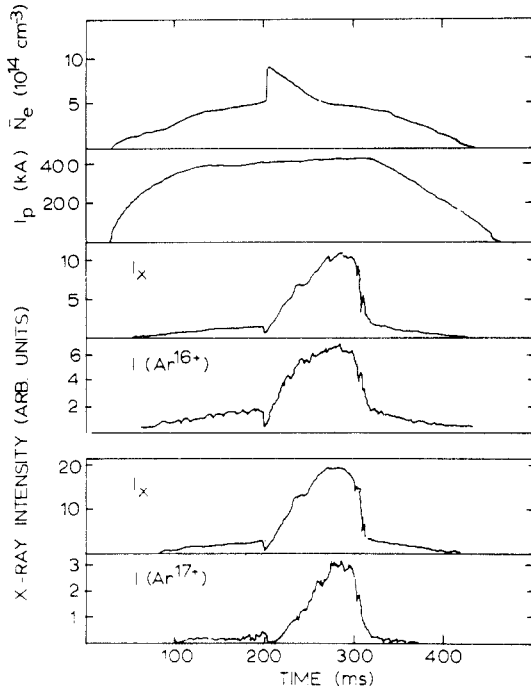


Fig. 14. The observed spectrometer count rate for plasma discharges with pellet injection for two wavelength regions: (a) $\lambda = 3.9\text{--}4.1\text{ \AA}$ representing the He-like spectrum of Ar ($I(\text{Ar}^{16+})$) and (b) $\lambda = 3.6\text{--}3.8\text{ \AA}$ representing the H-like spectrum ($I(\text{Ar}^{17+})$). Comparison is made with the soft X-ray signal (I_x), the plasma current (I_p) and the line integrated density (\bar{N}_e).

discharges with very low seeding levels, we have combined the data from several similar discharges. The results of each spectrum of Fig. 15 represent a time bin of 20 ms and the pellet was injected during the end of spectrum number 11. We observe that line ratios J/W , k/w , q/w and G show an increase in spectra nos. 11 and 12, indicating the decrease in T_e . For q/w , k/w , G and J/W we observe minimum values in the post injection region which show that T_e not only recovers but that the pre-injection temperature level is exceeded. Finally, the shallow minimum in the time history of $G(t)$ is consistent with the very weak temperature dependence of this line ratio. Thus, all these line ratios show a systematic pattern in their time development, demonstrating a common dependence on T_e .

The main feature of $R(t)$ is the minimum in the post-injection region being some 40% lower than the level before the injection. This corresponds to a factor of four change in density and hence is consistent with the central density increase caused by the pellet. We may note that the R value of spectrum 12 remains above the minimum value although N_e would already have reached its maximum value at this point. In this interval of rapid change in T_e , however, one cannot expect R to reflect only N_e since ionization and recombination are likely to be further out of balance than normal. This would affect R because of the different recombination contributions to triplet and singlet states [31, 33].

The results on the line widths show a rather smooth development with time, but the present time resolution of 20 ms is marginal for detecting any rapid change at the time of pellet injection. Apart from the transition region, the line width data for both H- and He-like spectra show a correlation in the T_e dependent line ratios. One may also note a possible difference in the data on $\Gamma_w(t)$ and $\Gamma_{w1}(t)$ which could arise because of the different radial profiles of the He-like and H-like states; they are both peaked at the center, but the H-like radial distribution is narrower.

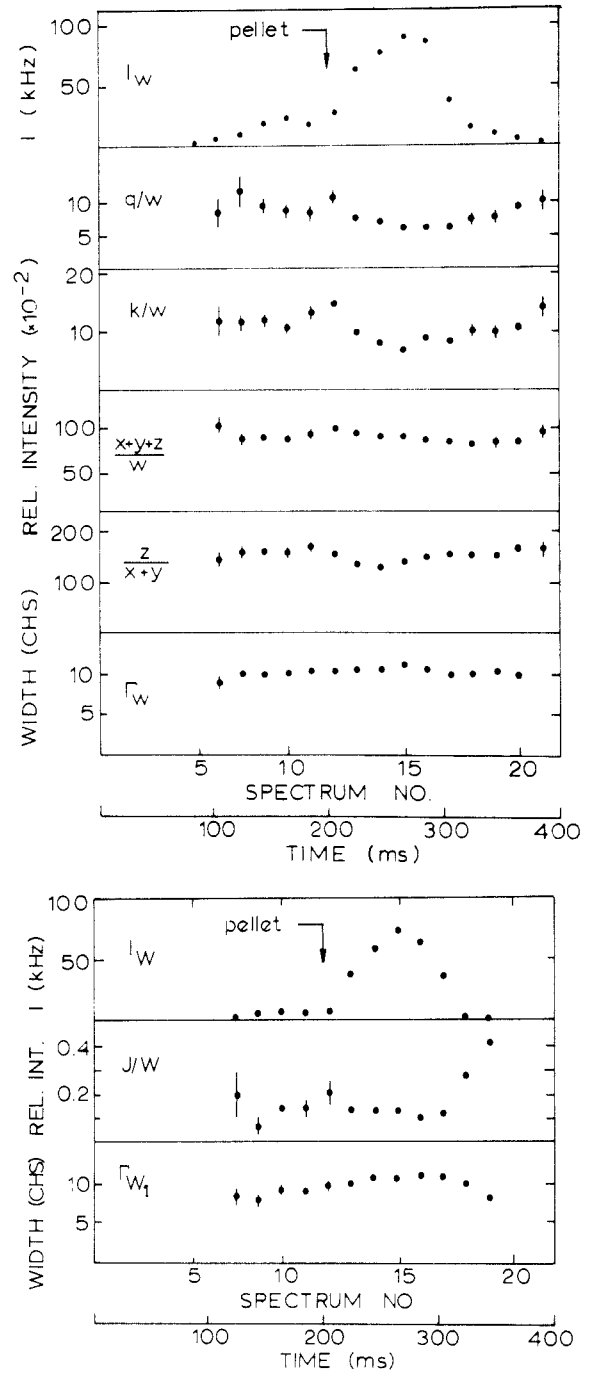


Fig. 15. The time dependence of the measured count rate, line intensity ratios and line widths observed in (a) the He-like and (b) H-like spectra of Ar for plasma discharges with pellet injection.

Examples of results for $T_i(t)$ and $T_e(t)$ deduced from Γ_w and k/w from a single discharge shown in Fig. 16. With a time resolution of 20 ms, we can clearly detect the drop in $T_e(t)$ at the time of the pellet injection; the results on T_i show no obvious change at the time of the injection. Also recorded by the x-ray emission is the post-injection maximum in $T_e(t)$.

4.6 Radial Scan Measurements

The brightness curves $I(d)$ of the lines W, w and q for the charge states Ar^{17+} , Ar^{16+} and Ar^{15+} are shown in Fig. 17; these extend over more than three orders of magnitude for d between 0 and 12 cm. All three transitions appear with intensities that decrease with increasing radius but at different rates. We note some decrease in the ratio $I_w(d)/I_w(d)$ between $d = 0$ and $d = 5$ cm, but beyond this there appears to be no substantial change which is in sharp contrast to the continued decrease which would be obtained if the plasma were in coronal equilibrium. This

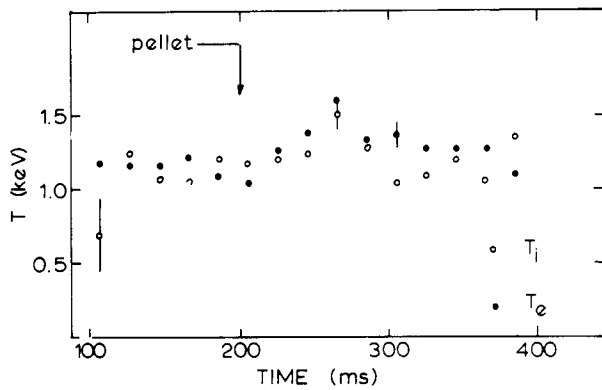


Fig. 16. Results on electron (T_e) and ion (T_i) temperature using the data on the line intensity ratio k/w and the line width Γ_w accumulated in five similar discharges.

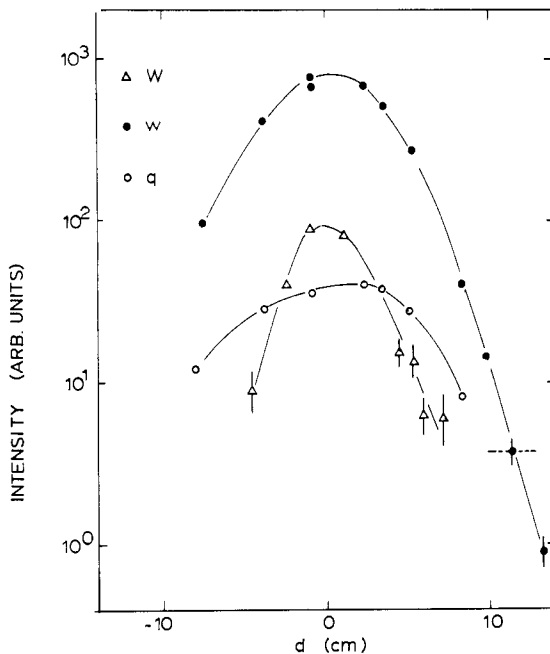


Fig. 17. The relative brightness measured as a function of distance from the plasma axis for the resonance lines $W_{1,2}$ of Ar^{17+} , the resonance line w of Ar^{16+} and the inner-shell excitation line q of Ar^{15+} .

difference implies that the ion charge state ratios are affected by ion transport effects as well as by the recombination/ionization rate balance. This trend is enhanced when extrapolated to the region $d \lesssim 13$ cm. The redistribution of the ion charge states has consequences for the relative weights of the competing population mechanisms; this can be seen in the data on relative line ratios.

Examples of He-like Ar spectra measured for chord heights between $d = -7$ cm and 13 cm are shown in Fig. 18 a-c. The central chord spectrum shown in Fig. 18a is typical for plasma conditions of $T_e \approx 1.4$ keV. An example of enhanced relative satellite intensities due to lower electron temperature ($T_e \approx 600$ eV) is shown by the spectrum measured by $d = 8.3$ cm (Fig. 18b). The He-like spectrum observed at $d = 12.8$ cm shows a dramatic change in relative intensities of the principal lines due to a change in population mechanism (Fig. 18c). The relative satellite intensities are also much smaller in this spectrum. Results of relative line intensities as functions of d are summarized in Fig. 19 in terms of line ratio combinations S , G , K , k/w and q/w . The line ratios k/w and q/w indicate that a change

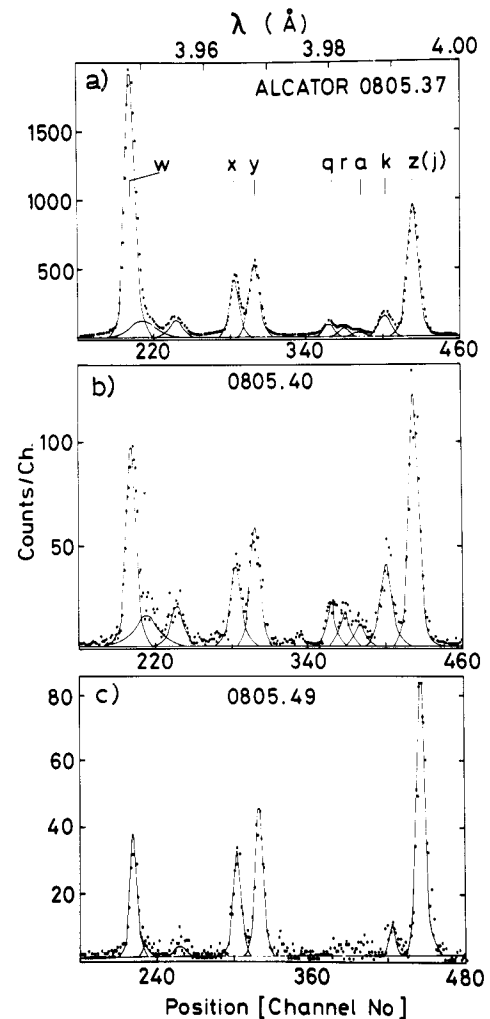


Fig. 18. The He-like spectrum of Ar recorded for three different lines of sight at chord distances of $d = -0.7$ (a), $d = 8.3$ (b) and $d = 11.3$ cm (c) from the plasma axis.

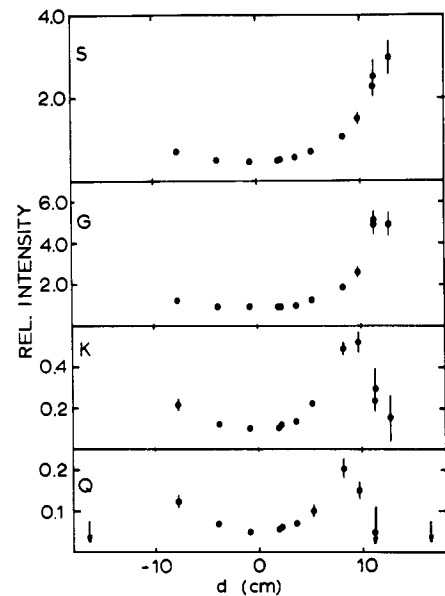


Fig. 19. The line intensity ratios $S = (x + y)/w$, $G = (x + y + z)/w$, $K = k/w$ and $Q = q/w$ of the He-like Ar spectrum measured as a function of the distance d from the plasma axis. The limiter radius was 16.5 cm as indicated by the arrows.

in population takes place at $d \approx 9$ cm where electron impact excitation and dielectronic recombination processes are replaced

as dominant population mechanisms by radiative and charge transfer recombination. The change from population by inner shell excitation to recombination requires the $N(\text{Ar}^{17+})/N(\text{Ar}^{16+})$ abundance ratio to exceed $2 \cdot 10^{-3}$ which indeed is consistent with the extrapolation made from the measured I_W/I_w ratio (Fig. 17).

4.7 Intensity Ratios for Fine Structure Transitions

The line intensity ratios for W_2/W_1 and x/y belonging to the $2^2P_{1/2, 3/2}$ and $(1s2p) 2^3P_{2, 1}$ states respectively, are predicted to be 0.5 and 0.78. Generally, the experimental results are consistent with these theoretical values although exceptions have been observed both for tokamaks and astrophysical plasmas [28, 34]. Theoretical attempts have been made to find an explanation [34, 35]. In the present experiment we again observe odd ratios of x/y and W_2/W_1 and we have also looked for systematic trends in the temporal or radial dependences measured. In the time dependence of W_2/W_1 we find a tendency of decreasing values towards the beginning of the discharge where the plasma is in a state of building up density and temperature. The x/y line ratio shows no systematic variation with time. In the radial scan data, we find no large systematic variation in either of these line ratios.

5. Discussion

We have presented results obtained with a new spectrometer system and demonstrated the plasma diagnostic capabilities represented by the measured H- and He-like spectra for argon. The spectrometer, however, is equally suited for measuring the same spectra for other elements; for instance, by choosing Z -values in the range $Z = 14 - 30$, which can be done by using plasma seeding, the x-ray emission properties can be matched to the plasma electron temperatures in the range $T_e \approx 1 - 10$ keV. Suitable crystals are available with $2d$ -values in the range $2d = 2.5$ to 7 \AA so that the desired λ -range can be covered by Bragg angles in the range $\theta = 20$ to 40° which can easily be accommodated with the used spectrometer geometry. Examples of spectra through part of the H- and He-like iso-electronic sequences are shown in Figs. 20 and 21. These spectra show the same line structure features but there are specific systematic Z -dependences in the relative position of the satellites and also in the relative intensities of the principal lines, especially x/y , and of satellites.

Because of the difference in temperature of maximum emission for the H- and He-like spectra, for instance $T_m = 2.8$ and 1.8 keV, respectively, for Ar, measuring them simultaneously extends the working T_e range of the x-ray diagnostic. This would augment the dynamic range of the measurement (as discussed in section 2.4) so that better than 10% statistical accuracy could be maintained over a wide range of plasma conditions over which the emissivity of the H- or He-like x-ray lines changes by up to four orders of magnitude. A large bandwidth spectrometer would therefore allow the recording of the time history of a plasma discharge over large temperature ranges and radial profiles covering large radial temperature gradients.

Besides the increased dynamic range and general precision that accompany the simultaneous measurement of the H- and He-like spectra, such measurements are also of importance for the determination of T_e from the x-ray data. As was pointed out in section 3, T_e can be extracted from several line intensity

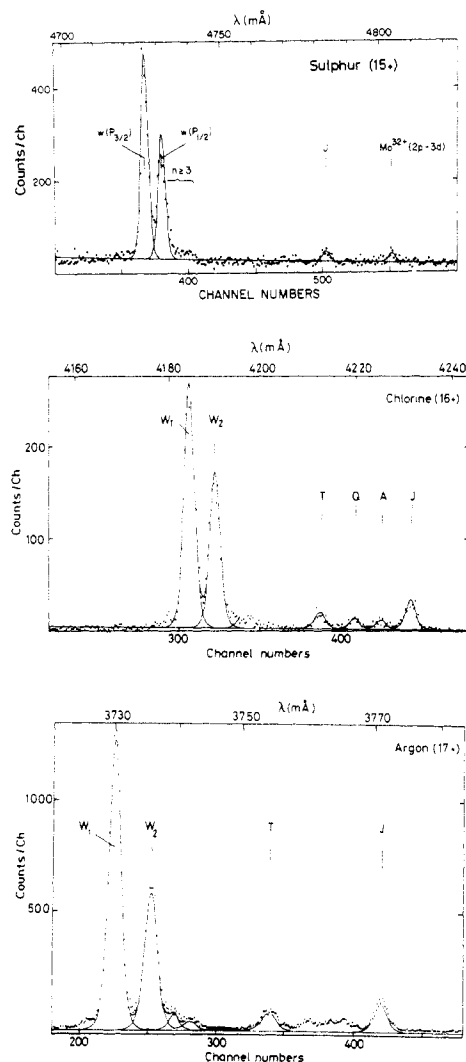


Fig. 20. Example of iso-electronic sequence of H-like spectra generated in plasmas of $\bar{N}_e \approx 3.10^{14} \text{ cm}^{-3}$ and $T_e \approx 1.3$ keV.

ratio combinations involving the resonance lines (w and W), and the dielectronic (k and J) and inner shell (q) satellites. However, simultaneous data on W/w , J/W , k/w and q/w are desirable for studying possible model dependent effects in the analysis for extracting T_e values from the individual ratios and would result in comprehensively determined T_e values of high accuracy. Since the ion temperature is reliably determined from the Doppler broadening, x-ray spectroscopy is a potential diagnostic of both T_e and T_i . The exploitation of this possibility appears interesting in view of the frequent observations of large T_e and T_i differences in tokamak plasmas. This question needs more experimental documentation for understanding of the thermal conductivity and other effects with a bearing on $T_e - T_i$.

The simultaneous measurement of H- and He-like spectra requires a bandwidth of about 10%. This can be obtained with the present spectrometer geometry by using a crystal with a length of 5 to 8 cm (the practical size limit being about $10 \times 15 \text{ cm}^2$) with a radius of curvature in the range of 35 to 60 cm. The overall dimensions of such a broad band spectrometer can still be kept small so as to retain the same flexibility as for the presently used instrument. The spatial resolution of the detector would ensure that a spectral resolution of better than $\delta\lambda/\lambda \leq 1/3000$ could be maintained even over the larger detector area required. The light collection efficiency, on the other hand, would be increased by a factor of 50 so that even

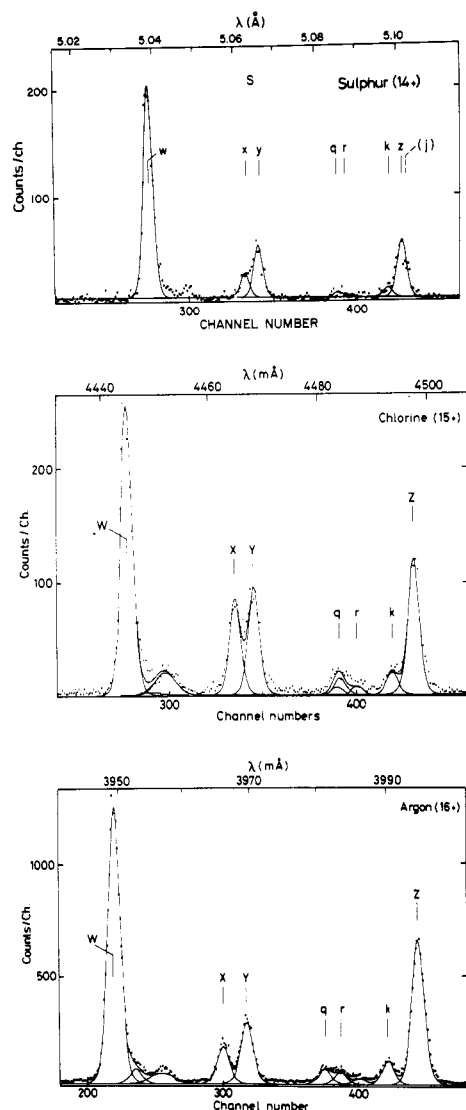


Fig. 21. Example of iso-electronic sequence of He-like spectra generated in plasmas of $N_e \approx 3 \cdot 10^{14} \text{ cm}^{-3}$ and $T_e \approx 1.3 \text{ keV}$.

to achieve count rates in excess of 1 MHz, the ion concentrations would never have to be raised above $N_i/N_e = 10^{-4}$ at $N_e \geq 10^{14} \text{ cm}^{-3}$. Furthermore, the instrument is relatively simple, so that several spectrometers could affordably be used at the tokamak for simultaneous multi-chord measurements. This would provide single shot information on the radial profiles of plasma parameters, for instance $T_i(r)$ and $T_e(r)$. The multi-chord measurements would be particularly powerful in combination with the broad bandwidth because of the different radial emissivities of the H- and He-like spectra. The same time resolved spectroscopic information for single discharges could be obtained that we have here demonstrated for consecutive discharges. However, a new and important aspect of these envisaged measurements would be the study of space and time correlation of spectroscopic data.

The present study was limited to the $n = 2$ to ground state transitions but some of the results on the recombination dominated spectra point directly to the interest for measuring the H- and He-like spectra involving transitions from the $n = 3$ or higher orbitals [31]. Similar information can be expected from the $n \geq 3$ to $n = 1$ as from the $n = 2$ to $n = 1$ spectra except for the absence of the intercombination line (y) and the forbidden line (z) in the $n \geq 3$ to $n = 1$ He-like spectra. The

intensity of the $n \geq 3$ to $n = 1$ spectra will generally be weaker with increasing n as far as population due to excitation processes goes. The $n \geq 3$ to $n = 1$ spectra are, therefore, useful in the case one wishes to suppress the sensitivity to high electron temperature excitation processes and favour low temperature capture reactions such as radiative or charge transfer recombination. The latter process is of great interest since it offers a possibility to probe the neutral content of the plasma. We have already estimated that the $n = 2$ to $n = 1$ spectrum is sensitive to the neutral content at a concentration level of $N_0/N_e > 10^{-5}$ and $T_e < 400 \text{ eV}$; these plasma conditions should occur outside some critical minor radius. These sensitivity limits could be extended towards higher T_e values and lower concentrations by measuring the x-ray transitions from orbitals which have the maximum charge transfer recombination rate. For argon, this is $n = 10$ [36]. In this case, the sensitivity should be essentially determined by the capture rate and the $N_0 \times N(\text{Ar})$ density product only while the contributions from competing processes would be effectively suppressed since their rates decrease with increasing n . X-ray spectroscopy of large Δn transitions could therefore be used for determining the radial distribution of neutrals in the plasma, particularly from the plasma edge region of high N_0 densities, and towards the plasma center with expected neutral density levels of $N_0 \approx 10^7 \text{ cm}^{-3}$ for typical Alcator conditions of $N_e = 2 \cdot 10^{14} \text{ cm}^{-3}$ and $T_e = 1.5 \text{ keV}$ [31]. Another possible measurement would be along lines of sight that intersect with the trajectory of pellets or neutral beams, in which case the capability of time resolved spectroscopy could be used for studying transient phenomena.

6. Conclusion

We have presented the design of an x-ray spectrometer suitable for use as a plasma diagnostic. The capabilities of this spectrometer were demonstrated in measurements of H- and He-like spectra of Ar at the Alcator C tokamak. New results were presented on ion (T_i) and electron (T_e) temperature as functions of time (t) and radius (r). The x-ray spectra from the peripheral parts of the plasma show effects of radial ion transport and dominant population by radiative and charge transfer recombination. The present experiment has demonstrated the capability to perform time resolved x-ray spectroscopy measurements with a time resolution of 10 ms. The next stage of spectrometer development is envisaged to incorporate large bandwidth ($\Delta\lambda/\lambda \geq 10\%$) and several spectrometers i.e., an x-ray instrument that can provide multi-parameter diagnostic information such as $T_i(r, t)$ and $T_e(r, t)$ for single tokamak plasma discharges.

Acknowledgements

This work was supported in part by the US Department of Energy. We wish to acknowledge the invaluable support by R. Parker and the Alcator group especially R. Gandy for ECE data and C. Fiore for neutral particle data and skillful computer programming done by Mr S. Magoon.

References

1. DeMichelis, C. and Mattioli, M., Nucl. Fusion **21** (1981) 677; and Rep. Progr. Phys. **47** (1984) 1233.

2. Bitter, M. et al., *Phys. Rev. Lett.* **43** (1979) 129 and *ibid* **42** (1979) 304.
3. Mewe, R. and Schrijver, J., *Astron. Astroph.* **65** (1978) 99 and *ibid* Suppl. Ser. **40** (1980) 323, and A.K. Pradhan and J.M. Shull, *The Astrophysical Journal* **249** (1981) 821 and A.K. Pradhan *ibid* **263** (1982) 477.
4. Gabriel, A.H., *Mon. Not. R. Astr. Soc.* **160** (1972) 99.
5. Hill, K.W., et al., *Phys. Scr.* **A19** (1979) 1770.
6. Bryzgunov, V.A., Yu Luk'yanov, S., Pakhomov, M.T., Potapov, A.M. and Chuvatin, S.A., *Sov. Phys. JETP* **55**, 6 (1982) 1095.
7. Platz, R., Ramette, J., Belin, E., Bonnelle, C. and Gabriel, A., *J. Phys.* **E14** (1981) 448.
8. Bartiromo, R., Bombarda, F. and Giannella, R., *Nucl. Instr. Meth. B*, 1985 to appear.
9. Lieber, A., Wojtowicz, S. West, W., *IEEE Int. Conf. on Plasma Science*, San Diego Calif. 1983 and A.J. Lieber, S.S. Wojtowicz and K.H. Burrell, GA-A17636 October 1984.
10. Källne, E., Källne, J. and Rice, J.E., *Phys. Rev. Lett.* **49** (1982) 330 and Källne, E., Källne, J. and Pradhan, A.K., *Phys. Rev.* **A27** (1983) 1476.
11. Källne, E., Källne, J. and Pradhan, A.K., *Phys. Rev.* **A28** (1983) 467.
12. Källne, E., Källne, J., Marmar, E.S. and Rice, J.E., *Nucl. Instr. Meth. B* 1985 (to appear).
13. Canizares, C.R., Clark, G.W. Markert, T., In *X-ray Imaging SPIE* **106** (1977) 157.
14. Bartiromo, R., Giannella, R. and Bombarda, R., *X-ray Crystal Spectrometer*, JET JB1/9000, ENEA report 1981 (unpublished).
15. Hamos, L.V., *Ann der Physik* **17** (1933) 716.
16. Källne, J., Källne, E., Atencio, L.G., Morris, C.L. and Thomson, A.C., *Nucl. Instr. Meth.* **203** (1982) 415 and to be published.
17. Greenwald, M. et al., *Phys. Rev. Lett.* **53** (1984) 352 and MIT Plasma Fusion Center Report PFC/JA-84-3 March 1984.
18. Fairfax, S. et al., *Proc. of 8th Int. Conf. on Plasma Physics and Controlled Nuclear Fusion Research IAEA*, Brussels, Vol. 1 p. 439 1980.
19. Post, D.E., Jensen, R.V., Tarter, C.B., Grasberger, W.H. and Lokke, W.A., *Atomic Data and Nuclear Data Tables* **20** (1977) 397.
20. Pradhan, A.K., Norcross, D.W. Hummer, D.G., *The Astrophysical Journal* **246** (1981) 1031.
21. Schnopper, H.W., Silver, E. and Westergaard, N.J., *Physica Scripta* **T7** (1984) 192 Yaakobi, B., Turner, R.E., Schnopper, H.W. Taylor, P.O., *Rev. Sci. Instr.* **50** (1979) 1609.
22. Källne, E. and Källne, J., *Physica Scripta* **T3** (1983) 185.
23. Källne, E. and Källne, J., *JET Report Dec. 1983* (unpublished).
24. Sauli, F., *CERN Report 77-09*, 1977 (unpublished).
25. Vainshtein, L.A. Safronova, U.I., *Atomic Data Nuclear Data Tables* **21** (1978) 49 and **25** (1980) 311; Safronova, U.I., Urnov, A.M. and Vainshtein, L.A., *Institute of Spectroscopy USSR Academy of Science Report 1982*, Safronova, U.K.I. Lisina, T.G., *Atomic Nucl. Data Tables* **24** 1979 (49) and Safronova, U.I. private communication.
26. Bitter, M. et al., *Phys. Rev. Lett.* **47** (1981) 921.
27. Feldman, U., *Physica Scripta* **24** (1981) 681.
28. Källne, E. and Källne, J., *AIP Conf. Proc. No.* **94** (1982) 463.
29. Marmar, E.S. et al., (to be published).
30. Brau, K., Goeler, S. von., Bitter, M., Cowan, R.D., Eames, D., Hill, K., Sauthoff, N., Silver, E. and Stodieck, W., *Phys. Rev.* **A22** (1980) 2769.
31. Källne, E., Källne, J., Dalgarno, A., Marmar, E.S., Rice, J.E. and Pradhan, A.K., *Phys. Rev. Lett.* **52** (1984) 2245.
32. Källne, E., Källne, J., Richard, P. and Stöckli, M., *J. Phys. B* **17** (1984) L115.
33. Pradhan, A.K., *The Astrophysical Journal*. To appear 1985.
34. Ljepojevic, N.N., Hutcheon, R.J. McWhirter, R.W.P., *J. Phys. B* **17** (1984) 3057.
35. Zygelman, B. and Dalgarno, A., to appear in the *Proceedings of the Symposium on X-ray and UV Spectroscopy*, Inst. Astronomical Union Meeting, Washington, August 1984 and McWhirter, R.W.P., private communication.
36. Janev, R.R., Belic, D.S. and Bransden, B.H., *Phys. Rev.* **A28** (1983) 1293.